Neural Networks 181 (2025) 106778

Contents lists available at ScienceDirect

Neural Networks

journal homepage: www.elsevier.com/locate/neunet

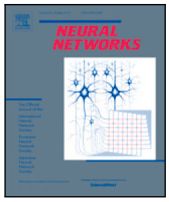

Full Length Article

A deep learning approach for non-invasive Alzheimer's monitoring using microwave radar data

Farhatullah [a], Xin Chen [b,*], Deze Zeng [a], Rahmat Ullah [c], Rab Nawaz [c], Jiafeng Xu [b], Tughrul Arslan [d]

[a] School of Computer Science, China University of Geosciences, Wuhan, 430074, China
[b] School of Automation, China University of Geosciences, Wuhan, 430074, China
[c] School of Computer Science and Electronic Engineering, University of Essex, Wivenhoe Park, Colchester, CO4 3SQ, Essex, United Kingdom
[d] School of Engineering, University of Edinburgh, Edinburgh EH8 9YL, UK

ARTICLE INFO

Keywords:
Alzheimer's disease
Classification
Deep learning
Data augmentation
Microwave scattering
Signal processing

ABSTRACT

Over 50 million people globally suffer from Alzheimer's disease (AD), emphasizing the need for efficient, early diagnostic tools. Traditional methods like Magnetic Resonance Imaging (MRI) and Computed Tomography (CT) scans are expensive, bulky, and slow. Microwave-based techniques offer a cost-effective, non-invasive, and portable solution, diverging from conventional neuroimaging practices. This article introduces a deep learning approach for monitoring AD , using realistic numerical brain phantoms to simulate scattered signals via the CST Studio Suite. The obtained data is preprocessed using normalization, standardization, and outlier removal to ensure data integrity. Furthermore, we propose a novel data augmentation technique to enrich the dataset across various AD stages. Our deep learning approach combines Recursive Feature Elimination (RFE) with Principal Component Analysis (PCA) and Autoencoders (AE) for optimal feature selection. Convolution Neural Network (CNN) is combined with Gated Recurrent Unit (GRU), Bidirectional Long Short Term Memory (Bidirectional-LSTM), and Long Short-Term Memory (LSTM) to improve classification performance. The integration of RFE-PCA-AE significantly elevates performance, with the CNN+GRU model achieving an 87% accuracy rate, thus outperforming existing studies.

1. Introduction

Dementia is the fifth primary cause of global mortality, a figure that increased from 20.2 million in 1990 to 43.8 million in 2016, based on clinical records (Nichols et al., 2019). Alzheimer's disease (AD) ranks as the most prevalent contributor, constituting 60%–80% of dementia cases, alongside Dementia with Lewy bodies (DLB), Frontotemporal dementia (FTD), vascular dementia (VD), and Parkinson's disease (PKD) (Polanco et al., 2018). Initially identified by Alois Alzheimer in 1906, AD manifests itself through a gradual deterioration in cognitive and behavioral faculties, marked by memory loss, aphasia, apraxia, agnosia, visual impairments, abstract thinking challenges, and cognitive deficits (Vishal, Sourabh, & Harkirat, 2011). Although precise pathological pathways for AD remain elusive, predominant theories implicate the hypothesis of the amyloid cascade and tau protein hyperphosphorylation (Bloom, 2014). AD instigates various physiological and pathological transformations in the brain, encompassing cerebral atrophy, enlargement of lateral ventricle, augmented cerebrospinal fluid (CSF) levels, and the emergence of amyloid plaques and neurofibrillary tangles.

Currently, conventional methods such as MRI and positron emission tomography (PET) are widely used to monitor neurodegenerative disorders. However, these imaging modalities are expensive, bulky, and often inaccessible to the elderly due to physical challenges (Ullah, Saied, & Arslan, 2022). In contrast, Microwave (MW) imaging offers a promising alternative, characterized by its portability and ease of use, making it better suited for frequent monitoring. Although initially explored for the detection of brain stroke and breast cancer, recent studies have explored their potential to identify physiological and pathological changes within the brain (O'Loughlin et al., 2018; Saied et al., 2020). Despite these advantages, MW imaging faces significant challenges, particularly its low spatial resolution, which hampers its ability to detect the subtle changes typical of the early stages of AD. This limitation is critical because early detection is important to monitor AD progression.

* Corresponding author.
E-mail addresses: farhatkhan8398@cug.edu.cn (Farhatullah), chenxin@cug.edu.cn (X. Chen), deze.zeng@ieee.org (D. Zeng), rahmat.ullah@essex.ac.uk (R. Ullah), rab.nawaz@essex.ac.uk (R. Nawaz), xujiafeng@cug.edu.cn (J. Xu), tughrul.arslan@ed.ac.uk (T. Arslan).

https://doi.org/10.1016/j.neunet.2024.106778
Received 18 June 2024; Received in revised form 7 September 2024; Accepted 1 October 2024
Available online 5 October 2024

Recent advancements in microwave (MW) technology coupled with deep learning algorithms offer a novel approach to the early detection and monitoring of Alzheimer's Disease (AD). Unlike traditional imaging techniques such as MRI and PET, MW imaging provides a cost-effective, non-invasive, and portable solution, making it particularly suitable for continuous monitoring in a home setting (Origlia, Rodriguez-Duarte, Tobon Vasquez, Bolomey, & Vipiana, 2024). The unique advantage of MW data lies in its ability to capture real-time changes in brain physiology with minimal discomfort to patients (Chiao et al., 2022). Although MW imaging faces challenges such as low resolution and high noise levels, modern ML techniques are capable of enhancing signal processing to extract meaningful patterns from this data. Consequently, the integration of MW technology with sophisticated deep learning models has the potential to revolutionize AD diagnostics by enabling earlier and more accessible detection of subtle pathological changes before significant symptoms manifest. This research seeks to explore and validate the effectiveness of this integration, addressing current technological limitations and advancing our understanding of its applicability in clinical practice.

The early detection of AD involves tracking changes in CSF and brain atrophy before symptoms manifest. Machine learning (ML) and Deep Learning (DL) techniques currently rely on imaging modalities such as MRI and PET to analyze various features such as gray matter densities, brain volume, and accumulation of cerebral amyloids in the hippocampus (Jo, Nho, & Saykin, 2019). However, these methods are dependent on imaging technologies. Recently, a lightweight and non-invasive MW imaging device has been proposed to diagnose neurodegenerative diseases (Saied & Arslan, 2020). Despite its promise, the device generates low-resolution images due to a low signal-to-noise ratio, attributed to the radiation pattern of a wideband antenna, causing spatial blurring and signal scattering in tissues. More advanced signal processing techniques are necessary to improve the accuracy of monitoring or detecting the early stages of AD.

Machine learning (ML) has been proven to be effective in analyzing neuroimaging data in various diseases (Tsang, Xie, & Zhou, 2019), including stroke classification (Persson et al., 2014; Zhu, Bialkowski, Guo, Mohammed, & Abbosh, 2021). Current classification methods are successful in distinguishing intracerebral hemorrhage (ICH) from ischemic stroke (IS) and healthy individuals utilizing high-frequency MW data (Fhager, Candefjord, Elam, & Persson, 2018; Persson et al., 2014). However, there is untapped potential for ML to predict AD using MW data, which warrants further exploration. Previous studies have used data from pathological and physiological phantoms to classify multi-class AD (Saied, Arslan, & Chandran, 2022; Ullah, Dong, Arslan and Chandran, 2023; Ullah, Saied, & Arslan, 2021). However, these studies have identified several limitations that could impede the accuracy and reliability of AD predictions using MW data. Notably, the presence of outliers can significantly distort the predictive modeling process, leading to inaccurate AD diagnosis or misclassification. This is particularly critical as early detection of AD requires high precision to distinguish subtle changes that precede noticeable symptoms. Additionally, the common practice in previous research of treating all antenna data as a single signal sample for data augmentation can result in oversimplification of complex signal characteristics, thereby reducing the sensitivity of the model to early or mild forms of AD. Therefore, more sophisticated feature extraction methods are required to adequately capture and utilize the intricate patterns within MW data that are indicative of AD.

Deep learning techniques, despite their success in high-resolution neuroimaging, face significant challenges when applied to microwave (MW) imaging for Alzheimer's disease (AD) detection. Traditional models struggle with MW data's low resolution and high noise levels, which often obscure early-stage AD markers. Additionally, these models, typically optimized for static images, may not effectively process the dynamic data generated by MW sensors (Ullah, Saied and Arslan, 2023). To overcome these challenges, our research introduces a novel classification model that integrates advanced deep learning techniques specifically adapted for MW data. This model leverages Convolutional Neural Networks (CNNs) to extract spatial features and combines them with sequence modeling techniques, including Gated Recurrent Units (GRU) and Long Short-Term Memory (LSTM) networks, to capture temporal dependencies in AD progression. This hybrid approach enhances the detection of subtle physiological changes and supports continuous, non-invasive monitoring, making it well-suited for clinical and home-based applications.

The study also employs pre-processing techniques like normalization, standardization, and outlier removal to ensure data quality. This is important due to the inherent challenges, such as signal-to-noise ratio and the sparse nature of MW data for AD detection. These steps are essential for training robust deep learning models, enabling them to accurately identify subtle changes associated with early AD, thereby compensating for the limitations of MW imaging and ensuring reliable diagnostic performance. Data augmentation expands the dataset by treating each antenna's output as a distinct sample set. This approach is crucial as it allows for the capture and preservation of unique spatial information inherent to each antenna's location, enhancing the model's ability to detect regional variations in disease progression. Feature selection is optimized with Recursive Feature Elimination (RFE), and feature extraction is enhanced using Principal Component Analysis (PCA) and Variational Autoencoders (VAE). Finally, the combined use of CNNs, GRU, bidirectional-LSTM, and LSTM algorithms improves classification performance.

The main contributions of this research are as follows:

- Simulations are performed on realistic brain phantoms that mimic both physiological and pathological changes in the brain due to AD. These phantoms include various layers such as skin, skull, CSF, gray matter, and white matter. The scattering data from the simulations is captured and stored.
- Different preprocessing techniques are used to refine the data set, and a statistical measurement approach is used to augment the data for both physiological and pathological phantoms. The data collected from each antenna is treated as an individual sample. This enriches the data set and allows for a more comprehensive analysis.
- RFE is used to eliminate the least important features, and the resulting features are transformed into a new set of uncorrelated features using PCA. This effectively captures the maximum variance in the data. Additionally, variational autoencoders are utilized to enhance the feature representation, allowing for a comprehensive exploration of the latent features of the data set.
- Classification is performed based on different combinations of neural network algorithms. Convolution Neural Network is combined with Gated Recurrent Unit (GRU), Bidirectional- LSTM, and LSTM to improve classification performance.
- The obtained results are then evaluated using various metrics, including accuracy, precision, recall, and F1 score. These results are systematically compared with a previous study to assess the effectiveness of the proposed method.

The article's structure is as follows: Section 2 provides a comprehensive review of the existing literature, while Section 3 outlines the proposed methodology. Section 4 presents the results and engages in an in-depth discussion and comparative analysis of various algorithms, evaluating their accuracy and suitability in the context of AD monitoring. Finally, Section 5 concludes with a summary of the essential findings and outlines the directions for future research.

2. Literature review

Machine and deep learning strategies are being used to address the complex inverse scattering problem in microwave imaging. Previous work has used Artificial Neural Networks (ANN) (Rekanos, 2002) and

Support Vector Machines (SVMs) (Kerhet, Raffetto, Boni, & Massa, 2006) to extract various parameters from the MW scattering signals. DL methods in this context can be broadly categorized into three approaches: direct learning, learning-assisted objective function, and physics-assisted learning. One method, as described in Wei and Chen (2018), involves a direct learning approach that employs CNNs to compute the relative permittivity of scattered signals. However, this approach frequently results in suboptimal image quality. In contrast, the learning-assisted objective function approach combines networks to comprehend elements of conventional iterative solvers (Chen, Shah, Stang, & Moghaddam, 2019; Guo et al., 2019; Sanghvi, Kalepu, & Khankhoje, 2019). The field of physics-assisted learning methods (Guo et al., 2021; Li et al., 2018; Wei & Chen, 2019) refers to the incorporation of physical insights into the inputs or internal structures of a network. While these approaches offer significant advancements, the broader field of deep learning continues to evolve, introducing novel methods that may inform future developments in microwave imaging.

Recent advancements in deep learning provide a broader context for understanding potential improvements in MW imaging techniques. Techniques such as Multi-level Fusion and Attention-guided CNNs (Zhang, Wang, Luo, & Huang, 2020), Sparse Multiscale Radial Basis Function Networks combined with the Fisher Vector approach (Li et al., 2019), and Projective Parameter Transfer (Fei, Wang, Ying, Hu, & Shi, 2020) offer sophisticated feature extraction capabilities that can be used for enhancing signal clarity and accuracy. Deep active learning strategies (Zhang et al., 2021) and Hybrid Attention Dense Connected Networks (Chen et al., 2022) demonstrate the ongoing evolution of deep learning architectures that could be adapted to refine diagnostic models for complex medical applications like AD detection using MW signals.

Another ML-based MW method for breast lesion detection was introduced in Rana et al. (2019), using clinical data collected via a mobile transmitting and receiving antenna. The preprocessing of the MW scattering data involved leveraging previous research conducted by traditional radiologists on the same subjects. This preprocessed data, labeled accordingly, underwent training and evaluation using supervised ML techniques. Statistical analyses revealed that the SVM achieved an impressive 98% accuracy in detecting breast data. However, there were concerns about potential overfitting due to the reliance on only 36 frequency samples in the study. A recent study introduces a novel approach for the noninvasive detection of brain hemorrhage using a two-antenna system combined with machine learning classifiers (Singh et al., 2024). It uses simulated S-parameter data to distinguish the dielectric changes caused by hemorrhages. Research demonstrates that decision tree, KNN, and random forest classifiers outperform others in accuracy, precision, and recall to predict brain hemorrhage locations. A similar study evaluates the use of SVMs in classifying brain strokes through microwave technology (Pokorny et al., 2023). This study emphasizes the importance of training data characteristics. The study used extensive simulations to generate a synthetic dataset. The findings suggest that single-frequency data is effective in training SVMs for accurate stroke detection and classification.

A study by Zuo, Wu, Chen, Lei, and Wang (2024) introduced the Prior-Guided Adversarial Learning with Hypergraph (PALH) model, which utilizes multi-modality medical images and anatomical knowledge to predict abnormal brain connections. The model incorporates a hypergraph perceptual network to establish high-order relationships between modalities, providing valuable insights for early cognitive disease detection. Similarly, Zuo et al. (2023) proposed the Brain Structure-Function Fusing-Representation Learning (BSFL) model for analyzing mild cognitive impairment (MCI). This model uses a decomposition-fusion framework and a knowledge-aware transformer to capture both local and global brain connectivity. The fusion process is enhanced through a contrastive loss. In another study, Yu et al. (2022) developed the Multidirectional Perception Generative Adversarial Network (MP-GAN) model to visualize morphological features associated with AD severity. The model employs a multidirectional mapping mechanism and integrates multiple loss functions to generate class-discriminative maps and lesion visualizations consistent with clinical observations in different stages of AD.

A study by Saied et al. (2022) first explored the use of MW RF data for classifying AD. They utilize strategically positioned antennas to collect data that provides noninvasive insights into dielectric changes associated with Alzheimer's pathology. Various human models with different head sizes were measured and processed using a range of ML algorithms. The main objective of the study was to identify the most effective ML algorithm for classifying different stages of AD. The results indicated that the logistic regression model stands out, with an impressive accuracy of 98.97%, demonstrating its ability to distinguish between different stages of AD. This has significant implications in clinical and biological domains, offering a transformative application in clinics and monitoring systems. Integrating ML with noninvasive microwave medical sensors makes this approach a groundbreaking method for predicting Alzheimer's disease stages within the brain. However, the small number of observations serves as the main limitation of this method. In a similar study (Ullah, Dong et al., 2023) aimed at classifying different stages of AD, an ML-driven method was proposed. Numerical phantoms with diverse mesh cell compositions were used to simulate different stages of AD. An innovative data augmentation method was employed to increase the dataset. Afterward, several statistical features were extracted for model training. The study also utilized an AE for automated feature extraction, which enhanced classification accuracy by revealing important latent features. Three different classification algorithms were trained using the features extracted by the AE, and a comparative analysis was conducted against automatic and manually extracted features. The results showed that automatic feature extraction outperformed other methods, achieving an overall accuracy of 83% with the random forest classifier. This underscores the effectiveness of automatic feature extraction in enhancing the accuracy of AD stages classification.

A novel RF sensing system using eyeglasses to monitor blood flow variations non-invasively using backscattered RF signals is proposed in Anwar, Khan, Arslan, Russ, and Lomax (2024). The accuracy of the system in detecting flow rates between 10 and 90 mL/min is validated on an artificial brain model. Additionally, the system utilizes ML and DL methods to classify cerebral blood flow into low, average, and high categories. In a related study, Cardinali et al. (2023) apply a multilayer perceptron classifier to microwave sensing data from a multi-tissue head phantom that simulates different disease severities. They evaluate the binary classification performance across various hyperparameter settings and data subsets. Meanwhile, Hossain, Islam, and Almutairi (2022) use the YOLOv5 deep learning model in a portable microwave head imaging system to automatically detect brain abnormalities. The study assesses the performance of three YOLOv5 variants (YOLOv5s, YOLOv5 m, and YOLOv5l) using a dataset of 4400 radar microwave images.

The complexity of detecting various stages of AD Compared to identifying breast cancer and brain stroke, determining these conditions in the brain is more challenging due to its intricate structure (Ullah & Arslan, 2020). It is important to recognize that although MW methods are effective in detecting breast lesions, they face challenges when used for brain imaging due to the varied composition of brain tissues (Ullah & Arslan, 2021). Therefore, emphasizing feature extraction and classification in MW detection methods provides a promising approach for monitoring AD. Another obstacle is the limited availability of data, as there is still ongoing exploration of these systems and a lack of dedicated research on AD classification. Furthermore, the multidimensional nature of MW signals brings about complexities, which result in challenges such as the presence of redundant data and issues related to data singularity. These research gaps and the intricacies of data dimensions contribute to inefficiencies in classification techniques based on ML. Additionally, the signal from the target can be scattered by noise,

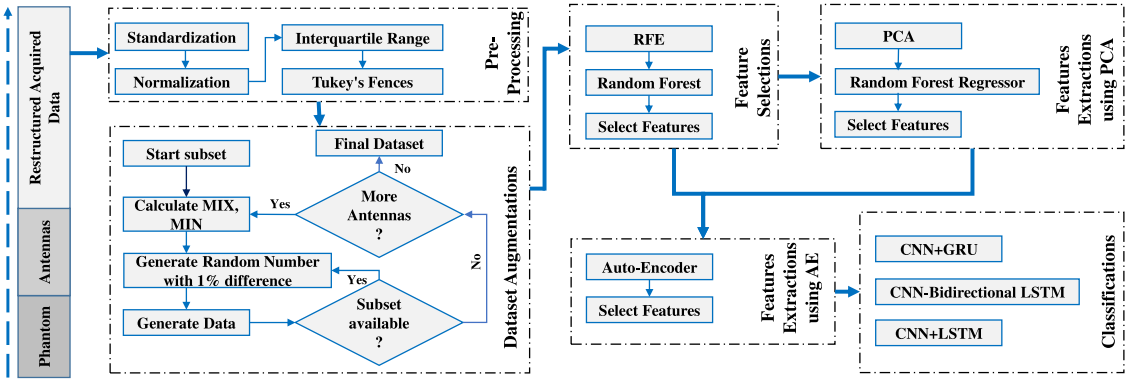

Fig. 1. Architecture of the proposed deep learning method. The architecture integrates raw data acquisition, preprocessing (transformation, feature fitness, data smoothing), beamforming, feature extraction (AFE, PCA), and classification models (CNN, GRU, Bidirectional LSTM, CNN-GRU-LSTM).

making detection more difficult due to subtle differences between the object being examined and the surrounding tissues (Rodriguez-Duarte et al., 2022). Therefore, achieving more accurate classification requires a comprehensive and integrated dataset and effective feature selection and extraction techniques, particularly those rooted in deep learning methodologies.

3. Material and methods

This section includes Data Acquisition and Preprocessing, which involve managing phantoms and antennas and preprocessing and re-structuring collected data. The Methods section includes augmentation, feature selection, feature extraction, and classification, as illustrated in Fig. 1. Each step includes several sub-steps, from acquiring the initial data to the final classification. This section aims to provide a comprehensive explanation of each of these steps.

3.1. Materials

3.1.1. Data acquisition and pre-processing

Obtaining data is a significant challenge for DL models because they require large datasets to achieve optimal accuracy. Because of their ease of use, PET and CT images are often used to train models. However, obtaining MW data is difficult because this technology is constantly emerging. This research focuses on human brain phantom data that replicate both healthy and AD brain. To do this, simulation models were developed using the CST MW Studio Suite, a specialist tool for 3D electromagnetic modeling (Ullah, Dong et al., 2023).

An advanced voxel model of the human head was used, incorporating various mesh cell configurations to generate phantoms to mimic different stages of AD. These phantoms were carefully designed to reflect the physiological and pathological changes associated with different stages of AD, using mesh cell sizes that correspond to varying head dimensions. Uniform reductions in mesh cell sizes were applied to represent brain atrophy, which includes shrinkage in both gray matter and white matter, to model physiological changes. An additional layer to simulate cerebrospinal fluid (CSF) was introduced while keeping the dimensions of other tissues (skull, skin) unchanged. Phantoms for mild and severe AD were developed by varying the thickness of the CSF layer and the degree of brain atrophy. For a mild AD condition, a 20% reduction in the volumes of white and gray matter was implemented from 2.23×10^6 mm^3 to 1.78×10^6 mm^3. Concurrently, there was a 20% increase in the volume of the CSF layer from 1.71×10^5 mm^3 to 2.05×10^5 mm^3

To simulate the pathological changes associated with Alzheimer's Disease (AD), this study leveraged findings from a comprehensive analysis of the dielectric properties of brain tissues, which are pivotal in understanding how AD affects electromagnetic signal interactions

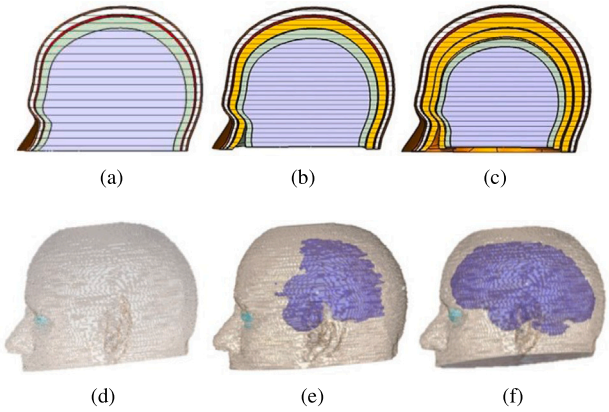

Fig. 2. CST head models illustrating physiological and pathological brain changes, referenced from our previous work (Ullah et al., 2021): (a) Healthy brain, (b) Mild AD with 10% brain atrophy, (c) Severe AD with 25% brain atrophy, (d) Healthy brain model, (e) Mild AD model depicting pathological changes, (f) Severe AD model depicting pathological changes.

within the brain. Previous research (Saied, Bashri, Arslan, Smith, & Chandran, 2019) revealed significant differences in dielectric properties between healthy brains and those affected by AD, highlighting the role of pathological changes in altering the composition and function of brain tissue. Specifically, this analysis focused on the relative permittivity and conductivity of gray and white matter in brains afflicted with severe AD compared to healthy counterparts. Measurements were carried out on defrosted tissue samples across a frequency range of 20 MHz to 3 GHz. The results revealed a pronounced decrease in the relative permittivity of gray matter from 53.3 in healthy brains to 45.3 in AD-affected brains at 770 MHz, marking a reduction of 15%. Similarly, an increase in conductivity was observed from 0.8906 S/m in healthy brains to 1.6253 S/m in AD brains at the same frequency, indicating a rise of 82. 5%. White matter showed a parallel trend, with relative permittivity dropping by approximately 17.61% and conductivity increasing by 26.72% in AD brains compared to healthy ones.

These pathological markers, beta-amyloid plaques, and tau tangles, significantly contribute to the deterioration of brain tissue in AD by impeding nutrient transfer within brain cells. The voxel models were meticulously developed to reflect the progression of these pathological changes, thereby facilitating a realistic simulation of how plaques and tangles spread throughout the brain as AD advances. The head models used for both physiological and pathological changes in simulation can be found in Fig. 2.

Six directional antennas arranged in a circular configuration around the head models were used to achieve comprehensive coverage. The

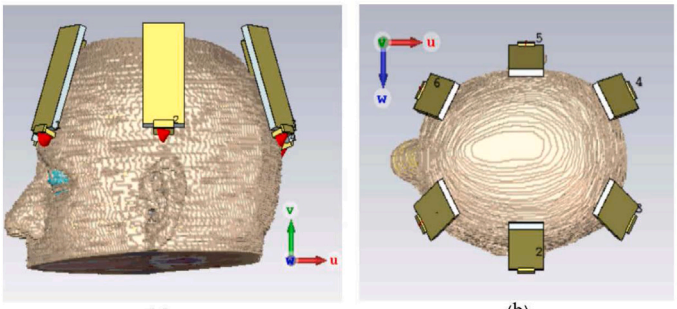

Fig. 3. Visualization of brain phantoms with surrounding RF antennas: (a) Front view of the brain phantom and six surrounding antennas, (b) Top view of the brain phantom with surrounding antennas.

Table 1
Data acquisition and reconstruction for AD classes. The raw data was acquired using six antennas and 200 discrete frequencies, processing of nine phantom compositions. The data is then restructured based on the antenna locations to produce the final dataset.

Classes	Raw data	Phantom compositions	Restructured data	Final data
Healthy	6 × 200	9 × 1200	54 × 200	
Mild	6 × 200	9 × 1200	54 × 200	162 × 200
Severe	6 × 200	9 × 1200	54 × 200	

simulations employed a multi-static approach, wherein each antenna transmitted MW signals sequentially while the remaining antennas captured the scattered signals. This process was repeated iteratively until a complete dataset of reflection coefficients from each antenna setup was compiled, focusing solely on the reflection coefficient data for analysis. Using various mesh configurations of brain phantoms, simulations were used to accommodate various head dimensions, ensuring a diverse data set. A model along with six surrounding antennas can be seen in Fig. 3. Further information about the antennas used and simulations can be found in Ullah, Dong et al. (2023).

The captured reflected signals, specifically the S-11 parameters in all antennas, provided a foundational data set to distinguish between different stages of AD: healthy, mild, and severe, encompassing both physiological and pathological aspects. A total of 200 frequency points were recorded in complex form for each antenna and later converted to absolute form as detailed in Table 1. Nine different phantom compositions were used to accommodate various head sizes, resulting in nine samples for each stage. The combined dataset for each stage consisted of 9 × 1200 points. The data was then reorganized to have 54 × 200 points for each stage, according to the antenna's location. Subsequently, the data were merged to create a final dataset of 162 × 200 data points.

3.2. Methods

3.2.1. Data augmentation

This section focuses on enhancing microwave-based data by introducing a novel data augmentation technique. The process involves multiple steps to augment the obtained S-parameters of healthy, mild, and severe classes. Importantly, augmentation is performed at the individual antenna level to avoid potential outliers that may occur when enhancing data across all antennas. Each antenna captures spatially distinct data due to its specific location relative to the brain, which may respond differently to the disease's progression. Treating each antenna's data separately allows for targeted augmentation that respects these spatial differences, thereby avoiding the introduction of potential outliers and preserving the integrity of spatial information. This approach ensures controlled randomness by introducing subtle variations in the data to increase the dataset's diversity. The proposed data augmentation method comprises several key steps. Initially, the resulting S-parameters' absolute values for each AD stage are first arranged into vectors. The data is then restructured based on antennas, acknowledging the similar nature of brain tissue across the same brain region in different cases. Subsequently, the data is divided into subsets of 5, and maximum and minimum values are computed for each subset. The subset of 5 is chosen for augmentation to make subsets of equal size, as each antenna consists of 200 data points. Furthermore, having a small subset preserves the original distribution's characteristics while introducing subtle variations. A random number within a specified percentage difference is then generated and included as a new data point. This procedure is repeated for each case and antenna, leading to a comprehensive augmentation. Algorithm 1 explains the steps of the proposed algorithm. Using this algorithm, a total of 500 instances were generated for healthy, mild, and severe cases, respectively.

Algorithm 1 Data Augmentation

Input:
Original Data: Original S-parameter data (O)
Number of Cases: Number of augmented cases (500)
Percentage Difference: Percentage difference for random number generation (default: 1%)
Output:
Augmented Data: Augmented S-parameter data
procedure DATA AUGMENTATION
    Create an empty list [Augmented Data] $|D|$
    for each i from 1 to number of cases **do**
        Create an empty list Augmented Cases $|C|$
        Calculate absolute values by taking the absolute values of $|O|$
        Reshape absolute values into a matrix Restructured data with dimensions (Number of Samples, 200)
        for each Subset start from 0, 5, 10, ..., 200 **do**
            Extract a subset of data from Restructured data
            Calculate the maximum and minimum values along each row of the subset
            Generate random numbers within 1% difference
            Append the generated random numbers to Augmented case
        end for
        Append $|C|$ to $|D|$
    end for
    return D
end procedure

3.2.2. Feature selection

After applying data augmentation, the RFE method is utilized for feature selection. RFE works iteratively by gradually removing less significant features from the dataset, resulting in a subset of the most informative features. This process improves model efficiency by reducing dimensionality while preserving essential features necessary for

Algorithm 2 Recursive Feature Elimination (RFE)

Input:
X: Initial dataset
k: Target number of features
Output:
X_k: Dataset with k selected features
procedure RFE(X, k)
    $X_0 \leftarrow X$ ▷ Initialize the dataset
    for $i = 0$ **to** $k - 1$ **do**
        $X_{i+1} \leftarrow \text{EliminateFeature}\left(X_i, \arg\min_k \left(\arg\max_w(\text{Model\_Performance}(X_i))\right)\right)$ ▷ Eliminate the least important feature
    end for
    return X_k ▷ Dataset with k selected features
end procedure

accurate classification. The detailed process is illustrated in Algorithm 2. The chosen subset, with relevant information, forms the basis for later stages, enhancing interpretability, computational efficiency, and model generalization. This methodical feature selection establishes the foundation for the following phases of the comprehensive approach to AD classification.

3.2.3. Feature extraction

After RFE, the methodology seamlessly advances to the feature extraction phase. Feature extraction, a key element of the proposed method, focuses on refining essential features. Two different methods are employed: RFE data is directly inputted into AE, and RFE data is first passed to PCA and then to AE. Initially, the RFE-selected features are input into PCA, which reduces dimensionality by transforming these features into a set of orthogonal variables that capture the most significant variance with minimal information loss. This transformation is crucial for enhancing computational efficiency and focusing the model on the most impactful data aspects. Subsequently, the PCA-processed data is fed into an Autoencoder, which excels in uncovering complex, hidden features through its neural network structure, designed to learn dense, latent representations. This approach allows for uncovering complex hidden features. This two-step feature extraction technique enhances the detection of distinctive patterns, enhancing the dataset with polished features necessary for accurate classification and staging of AD.

1. Principal Component Analysis (PCA) The selected features are subjected to PCA in order to refine the data. PCA, a technique for reducing dimensionality, transforms the original features into a new set of orthogonal variables called principal components. The main goal is to capture the maximum variance while minimizing the loss of information. By applying PCA to the feature subset obtained through RFE, the aim is to preserve relevant information while reducing the overall dimensionality. This enhances computational efficiency and helps alleviate the challenges posed by high-dimensional data. The transformed features generated by PCA serve as a concise and informative representation, contributing to the overall effectiveness of the proposed methods.
   The initial phase in the PCA process involves mean-centering the dataset. This is achieved by adjusting each feature value so that the mean of each is centered around the origin. This step is crucial for aligning the data in preparation for further analysis:

$$\bar{x}_j = x_j - \frac{1}{n}\sum_{i=1}^{n} x_i \tag{1}$$

   where $\bar{x}_j$ represents the mean-centered value of the jth feature, x_j is the original value of the j-th feature, n is the total number of observations, and $\sum_{i=1}^{n} x_i$ is the sum of all original values for the j-th feature across all observations.
   Following mean-centering, the covariance matrix C is computed. This matrix is vital as it uncovers the intricate relationships between the features of the mean-centered data, enabling the identification of patterns that are essential for dimensionality reduction:

$$C = \frac{1}{n}\sum_{i=1}^{n}(x_i - \bar{x})^{\top}(x_i - \bar{x}) \tag{2}$$

   Here, C represents the covariance matrix, x_i denotes a vector containing the mean-centered values for all features of the i-th observation, and $(x_i - \bar{x})^{\top}$ is the transpose of the mean-centered vector, ensuring that the matrix multiplication captures the relationships among all features.
   The next step involves the eigenvalue decomposition of the covariance matrix C. This procedure identifies the eigenvalues λ_i and their corresponding eigenvectors v_i. and their corresponding eigenvectors, which are the principal components that represent the directions of maximum variance in the dataset:

$$C \cdot v_i = \lambda_1 \cdot v_1 \tag{3}$$

   The transformation matrix W is then formed by selecting the top k eigenvectors based on the descending order of their corresponding eigenvalues. These eigenvectors are crucial as they define the new subspace onto which the original data will be projected:

$$W = [v_1\, v_2\, \ldots\, v_k] \tag{4}$$

   Finally, the original dataset is projected onto the newly defined subspace using the transformation matrix W. This results in a transformed matrix Y that contains the principal components. This last step is pivotal as it condenses the dataset while ensuring that the most important information is retained:

$$Y = X \cdot W \tag{5}$$

   Through this structured approach, PCA not only enhances the computational efficiency of the study but also effectively addresses the challenges posed by high-dimensional data, paving the way for the subsequent stages in AD classification. The Pseudocode of PCA can be found in Algorithm 3.
2. AutoEncoder (AE) Incorporating an Autoencoder (AE) into the feature extraction stage significantly enhances the process. An AE is a form of neural network designed to learn a condensed, latent representation of the input data, making it highly beneficial for tasks such as AD classification. This addition allows the extraction of complex patterns and subtle relationships within the data, focusing on identifying abstract features that may not be apparent in data already transformed by PCA. An AE operates through two main phases: encoding and decoding. In the encoding phase, the input data x is compressed into a smaller, dense representation h, utilizing weight matrices (W_e), bias terms (b_e),

Algorithm 3 Principal Component Analysis (PCA)

Input:
X: Data matrix with each row representing a sample and each column representing a feature
k: Number of principal components to retain
Output:
Data matrix in the reduced-dimensional space
procedure PCA(X, k)
    for each feature j **do** ▷ Standardize dataset
        $mean_j \leftarrow \text{mean}(X[:, j])$
        $std_j \leftarrow \text{std}(X[:, j])$
        $X[:, j] \leftarrow (X[:, j] - mean_j)/std_j$
    end for
    $CovarianceMatrix \leftarrow \text{Covariance}(X)$ ▷ Compute the covariance matrix
    $eigenvalues, eigenvectors \leftarrow \text{Eigendecomposition}(CovarianceMatrix)$ ▷ Eigenvalue decomposition
    $sorted\_indices \leftarrow \text{argsort}(eigenvalues)$ ▷ Descending order
    $top\_k\_indices \leftarrow sorted\_indices[1 : k]$
    $top\_k\_eigenvectors \leftarrow eigenvectors[:, top\_k\_indices]$ ▷ Top k eigenvectors
    $ProjectedData \leftarrow X \cdot top\_k\_eigenvectors$
    return $ProjectedData$
end procedure

and activation functions (f). Conversely, the decoding phase aims to reconstruct the input from this encoded form, generating an output r. The difference between the original input and the reconstructed output is quantified using a loss function $L(x, r)$, which serves as a measure of dissimilarity. The objective is to minimize this loss, effectively adjusting the encoder's and decoder's weights (W_e and W_d) to capture the most salient features of the input data within the compressed representation. The process of encoding the input data x into a compressed latent representation h using weight matrices W_e, bias b_e, and activation function f is given by:

$$h = f(W_e \cdot x + b_e) \tag{6}$$

The decoding phase, which aims to reconstruct the original input from the compressed representation h, resulting in output r, follows as:

$$r = f(W_d \cdot h + b_d) \tag{7}$$

The loss function $L(x, r)$, measuring the dissimilarity between the original input x and the reconstructed output r, is calculated using the squared error:

$$L(x, r) = \|x - r\|^2 \tag{8}$$

Finally, the objective of training the AE is to minimize this loss function, which is given by:

$$\min_{W_e, W_d} L(x, r) \tag{9}$$

By employing both PCA and AE in sequence, our approach utilizes the strengths of linear and nonlinear transformations to maximize the efficacy of our AD classification model. Initially, PCA aids in reducing the dimensionality of the pre-processed feature set, emphasizing the most informative features through linear methods. This reduction sets a solid foundation by highlighting principal components that encapsulate the most significant variance within the dataset, thereby simplifying the data's complexity and making the feature set more manageable and focused. Subsequently, the Autoencoder builds upon this linearly transformed data. AE is crucial for encoding higher-order interactions and complex, nonlinear relationships within the data, which are essential for capturing subtle and intricate patterns that linear methods like PCA may overlook. This nonlinear transformation is particularly important for detecting nuanced variations characteristic of different stages of AD, significantly enhancing the accuracy and sensitivity of our classification model.

3.3. Classification

Three alternative algorithms are used in combination to classify the best features: CNN+GRU, CNN + Bidirectional LSTM, and CNN+LSTM. Each configuration is specifically designed to capture different aspects of the data—CNN+GRU focuses on rapidly changing signal patterns, making it ideal for detecting abrupt changes in MW signals. CNN+Bidirectional LSTM, by processing data sequences in both forward and backward directions, provides a comprehensive analysis of temporal patterns, enhancing the ability to recognize progressive changes indicative of AD. Lastly, the CNN+LSTM setup is optimized to capture long-term dependencies in the signal data, crucial for identifying sustained trends over time. These combined approaches not only allow for robust extraction of meaningful patterns from complex MW signals but also ensure that the classification process is sensitive to both immediate and evolving indicators of AD, thereby improving diagnostic accuracy and reliability. Each model's architecture is described in depth below, along with the many configurations that were used for classification.

3.3.1. Convolution Neural Network and Gated Recurrent Unit (CNN-GRU)

The architecture of the CNN-GRU model is designed with distinct layers to efficiently process sequential data for classification tasks. The initial Convolutional Layer (Conv1D) has 64 filters with a kernel size of 3, and it uses Rectified Linear Unit (ReLU) activation functions to introduce non-linearity. The Max-Pooling Layer (MaxPooling1D) follows down-sampling spatial dimensions with a pool size of 2 to focus on salient features. Then, the Gated Recurrent Unit (GRU) Layer with 64 units is implemented, including dropout regularization of 0.2 for input and recurrent connections and a recurrent dropout rate of 0.2 to mitigate overfitting. The subsequent dense layer further refines the learned features with 64 units and ReLU activation. To enhance model generalization, a Dropout Layer with 0.5 is applied. The Flatten Layer reshapes the output to be compatible with the final Dense Layer, which has units equal to the number of target classes. The final density layer uses A Softmax activation function to produce class probabilities. This carefully designed architecture effectively captures spatial and temporal dependencies in sequential data, making it well-suited for multi-class classification tasks. The detailed architecture is further outlined in Table 2.

$$\text{Conv1D}(x) = \text{ReLU}(\text{Conv}(x, W_{\text{conv}}) + b_{\text{conv}}) \tag{10}$$

This equation represents the 1D convolutional operation applied to the input x. The convolution operation is performed using weights

Table 2
Architecture and parameter summary of the CNN-GRU model.

Layer type	Output shape	Parameters
Input layer	(32, 40, 1)	0
Conv1D layer	(32, 38, 64)	256
ReLU activation 1	(32, 38, 64)	0
MaxPooling1D layer	(32, 19, 64)	0
GRU layer	(32, 64)	24,960
Dropout layer (0.2)	(32, 64)	0
Dense layer 1	(32, 64)	4160
ReLU activation 2	(32, 64)	0
Dropout layer (0.5)	(32, 64)	0
Flatten layer	(32, 64)	0
Dense layer 2	(32, 3)	195
Softmax activation	(32, 3)	0
Total parameters:	**29,571**	

Table 3
Architecture and parameter summary of the CNN+bidirectional LSTM model.

Layer type	Output shape	Parameters
Input layer	(32, 40, 1)	0
Convolutional (Conv1D)	(32, 38, 64)	256
Bidirectional LSTM 1	(32, 128)	98,816
Bidirectional LSTM 2	(32, 64)	49,408
Dense layer 1	(32, 64)	4160
Dropout layer	(32, 64)	0
Flatten layer	(32, 64)	0
Dense layer 2	(32, 32)	2080
Dense layer 3 (Output)	(32, 3)	99
Softmax activation	(32, 3)	0
Total parameters:	**154,819**	

W_{conv} and a bias term b_{conv}. The result of this convolution is then passed through a Rectified Linear Unit (ReLU) activation function, which introduces non-linearity into the model.

$$M_{i\in\text{pool}}(x_i) \tag{11}$$

The MaxPooling1D operation reduces the spatial dimensions of the input x by selecting the maximum value from each pooling window. This process helps to highlight the most significant features while down-sampling the input data, making it more manageable and less prone to overfitting.

$$z_t = \sigma\left(w_z \cdot [h_{t-1}, x_t] + b_z\right) \tag{12}$$

The update gate z_t determines how much of the previous hidden state h_{t-1} should be retained. It is computed by applying a sigmoid activation function σ to a linear combination of the previous hidden state h_{t-1} and the current input x_t, along with a bias term b_z.

$$r_t = \sigma\left(w_r \cdot [h_{t-1}, x_t] + b_r\right) \tag{13}$$

The Reset Gate r_t decides how much of the previous hidden state should be forgotten. It is calculated using an activation function applied to a linear combination of the previous hidden state and the current input x_t, along with a bias term b_r.

$$\tilde{h}_t = \tanh\left(w_h \cdot [r_t \odot h_{t-1}, x_t] + b_h\right) \tag{14}$$

The candidate hidden state $\tilde{h}_t$ represents the new information to be added to the hidden state. It is computed by applying the hyperbolic tangent (tanh) activation function to a combination of the reset gate r_t, the previous hidden state h_{t-1}, the current input x_t, and a bias term b_h.

$$h_t = (1 - z_t) \odot h_{t-1} + z_t \odot \tilde{h}_t \tag{15}$$

The final hidden state h_t is a combination of the previous hidden state h_{t-1} and the candidate hidden state $\tilde{h}_t$. The update gate z_t controls the interpolation between these two states. If z_t is close to 1, the hidden state is updated to $\tilde{h}_t$; if z_t is close to 0, the previous hidden state h_{t-1} is retained.

$$\text{GRU}(x) = \text{GRU\_cell}(x, W_{\text{gru}}, U_{\text{gru}}, b_{\text{gru}}) \tag{16}$$

This concise equation represents the overall operation of the GRU layer using a GRU cell. It abstracts the detailed computations into a single function that takes the input x, along with the weights W_{gru}, recurrent weights U_{gru}, and biases b_{gru}.

$$y = \sigma(W \cdot x + b) \tag{17}$$

The dense layer performs a linear transformation of the input x using weights W and biases b. The result is then passed through an activation function σ, introducing non-linearity into the model. Additionally, dropout is applied with a probability p, where units are randomly set to zero during training with the specified dropout rate to prevent overfitting.

$$\text{dropout}(x, p) \tag{18}$$

The Dropout Layer randomly sets a fraction p of the input units x to zero during training. This helps prevent the model from becoming overly reliant on any single neuron and reduces overfitting. The parameter p represents the dropout rate, which is the proportion of units to drop out.

$$\text{Flatten}(x) \tag{19}$$

The Flatten Layer reshapes the input tensor x into a 1D vector. This transformation is necessary to feed the data into fully connected (Dense) layers.

$$\hat{y} = \text{Softmax}(y) \tag{20}$$

The Softmax Activation function converts the raw output scores y from the final Dense Layer into class probabilities. It computes the exponential of each score and normalizes these values by dividing by the sum of all exponentials

3.3.2. Convolution neural network and bidirectional long short term memory

The bidirectional LSTM model architecture begins with a Convolutional Layer (Conv1D) with 64 filters and ReLU activation. It is then followed by a MaxPooling layer (MaxPooling1D) to emphasize important features. Two bidirectional LSTM layers process the sequence, with the first layer having 128 units and the second layer having 64 units. A Dense Layer with 64 units and ReLU activation introduces non-linearity. Dropout with a rate of 0.5 is implemented to address overfitting, and a Flatten Layer is used to prepare for subsequent Dense Layers. The second Dense Layer consists of 32 units with ReLU activation, leading to the final Dense Layer with Softmax activation. The number of units in the final Dense Layer equals the number of classes. This architecture combines convolutional and bidirectional LSTM layers to effectively capture spatial and temporal dependencies, resulting in effective multi-class classification. The detailed architecture for CNN+Bidirectional is further outlined in Table 3. Mathematically, the Bidirectional LSTM forward pass is described by the equations from (21) to (26), while the backward pass is detailed in Eqs. (27) to (32).

$$f_t^f = \sigma\left(W_f \cdot [h_{t-1}^f, x_t] + b_f\right) \tag{21}$$

$$i_t^f = \sigma\left(W_i \cdot [h_{t-1}^f, x_t] + b_i\right) \tag{22}$$

$$\tilde{C}_t^f = \tanh\left(W_c \cdot [h_{t-1}^f, x_t] + b_c\right) \tag{23}$$

$$C_t^f = f_t^f \odot C_{t-1}^f + i_t^f \odot \tilde{C}_t^f \tag{24}$$

$$h_t^f = O_t^f \odot \tanh(C_t^f) \tag{25}$$

$$O_t^f = \sigma\left(W_o \cdot [h_{t-1}^f, x_t] + b_o\right) \tag{26}$$

The forward LSTM processes input sequences from the beginning to the end. At each time step t, the forget gate f_t^f determines which information to discard from the cell state C_{t-1}^f. The input gate i_t^f updates the cell state with new candidate values $\tilde{C}_t^f$, and the output gate O_t^f produces the hidden state h_t^f, which reflects the relevant information from the cell state.

$$f_t^b = \sigma\left(W_f \cdot [h_{t+1}^b, x_t] + b_f\right) \tag{27}$$

$$i_t^b = \sigma\left(W_i \cdot [h_{t+1}^b, x_t] + b_i\right) \tag{28}$$

$$\tilde{C}_t^b = \tanh\left(W_c \cdot [h_{t+1}^b, x_t] + b_c\right) \tag{29}$$

$$C_t^b = f_t^b \odot C_{t+1}^b + i_t^b \odot \tilde{C}_t^b \tag{30}$$

$$h_t^b = O_t^b \odot \tanh(C_t^b) \tag{31}$$

$$O_t^b = \sigma\left(W_o \cdot [h_{t+1}^b, x_t] + b_o\right) \tag{32}$$

The backward LSTM processes input sequences from the end to the beginning, capturing future context. At each time step t, the forget gate f_t^b manages the retention of information from the future cell state C_{t+1}^b. The input gate i_t^b integrates new information into the cell state using candidate values $\tilde{C}_t^b$, while the output gate O_t^b generates the hidden state h_t^b, incorporating the relevant information from the cell state. This version briefly describes the role of each gate in the backward LSTM. The combination of the forward and backward networks is shown in Eq. (33).

$$h_t = \left[h_t^f; h_t^b\right] \tag{33}$$

3.3.3. Convolution neural network and long short term memory

The CNN-LSTM model is designed to analyze robust sequential data and perform multi-class classification. This sophisticated architecture is composed of various layers, each tailored to perform specific functions that contribute to the model's overall ability to recognize complex patterns in the data. The first layer is an initial Convolutional Layer with 128 filters, a kernel size of 3, and ReLU activation. Following the Convolutional Layer, MaxPooling Layers are used to emphasize important features and downsize spatial dimensions, with a pool size set to 2. The model also includes two Bidirectional LSTM layers, with the first layer having 128 units and the second layer having 64 units. These LSTM layers effectively capture long-range dependencies in the data.

To introduce non-linearity and enhance the model's ability to learn complex patterns, a Dense Layer with 64 units and ReLU activation is added, complementing the LSTM layers. To counteract overfitting, a dropout layer with a rate of 0.5 is used in the model, preventing overreliance on the training data. The data is then passed through a Flatten Layer, preparing it for subsequent Dense Layers. A second Dense Layer with 32 units and ReLU activation precedes the final Dense Layer. The final Dense Layer uses Softmax activation to produce class probabilities. By combining convolutional and LSTM elements, this model effectively captures spatial and temporal complexities, making it well-suited for multi-class classification tasks. The comprehensive architecture and parameter details are presented in Table 4

$$f_t = \sigma\left(w_f \cdot [h_{t-1}, x_t] + b_f\right) \tag{34}$$

$$i_t = \sigma\left(w_i \cdot [h_{t-1}, x_t] + b_i\right) \tag{35}$$

$$\tilde{C}_t = \tanh\left(w_c \cdot [h_{t-1}, x_t] + b_c\right) \tag{36}$$

Table 4
Architecture and parameter summary of the CNN + LSTM model.

Layer type	Output shape	Parameters
Input layer	(32, 40, 1)	0
Convolutional (Conv1D)	(32, 38, 64)	256
ReLU activation 1	(32, 38, 64)	0
MaxPooling (MaxPooling1D)	(32, 19, 64)	0
LSTM 1	(32, 128)	49,280
LSTM 2	(32, 64)	41,920
Dense layer 1	(32, 64)	4160
ReLU activation 2	(32, 64)	0
Dropout layer	(32, 64)	0
Flatten layer	(32, 64)	0
Dense layer 2	(32, 32)	2080
ReLU activation 3	(32, 32)	0
Dense layer 3 (Output)	(32, 3)	99
Softmax activation	(32, 3)	0
Total parameters:	**97,795**	

$$c_t = f_t \odot c_{t-1} + i_t \odot \tilde{C}_t \tag{37}$$

$$o_t = \sigma\left(w_o \cdot [h_{t-1}, x_t] + b_o\right) \tag{38}$$

The LSTM network processes the input sequentially, where the forget gate f_t controls the retention of past information by deciding which parts of the previous cell state c_{t-1} to discard. Simultaneously, the input gate i_t updates the cell state with new candidate values $\tilde{C}_t$, determining which new information should be added. The cell state c_t is thus updated to reflect a combination of retained and newly introduced information. Finally, the output gate o_t determines the hidden state h_t by filtering the relevant information from the current cell state, which is used to predict the output for each time step.

4. Results and analysis

The proposed model was developed in Python using the SciPy library, which incorporates key Python libraries such as NumPy, Matplotlib, and Pandas. Various feature selection and extraction techniques were applied to the data, and the resultant features were then used in deep learning algorithms for classification purposes. The data set was divided into two subsets: 70% for modeling training and 30% for testing. The implementation was carried out on an HP Omen system equipped with a Core i9 processor, an RTX 4060 GPU with 12 GB of VRAM, and 32 GB of RAM. A range of evaluation metrics (including accuracy, precision, recall, and F1 score) were meticulously computed to ensure a thorough evaluation of the model's performance. These metrics collectively offer a comprehensive assessment of the model's efficacy in classification tasks, ensuring a detailed evaluation of their performance on the provided dataset.

In preprocessing, a comprehensive approach was implemented to enhance the quality of the data set, which is essential to ensure reliability and accuracy. Normalization and standardization were performed using the Min-Max and Standard Scalers to enhance the dataset's robustness. This process aimed to standardize the data for easier comparisons across different features. Following preprocessing, the focus shifted to removing outliers, an essential step for removing data points that might otherwise distort the analysis. Two methodologies were employed to achieve this: the Interquartile Range (IQR) and Tukey's Fences. Initially, the IQR method, which allows for sensitivity adjustments, was utilized to identify and remove outliers effectively. This was complemented by the application of Tukey's Fences, serving as an additional method to bolster the dataset's integrity. The results, depicted in Fig. 4, showcased the effectiveness of the pre-processing pipeline. Normalization, standardization, and outlier removal significantly improved the dataset's quality, establishing a solid foundation for further analyses

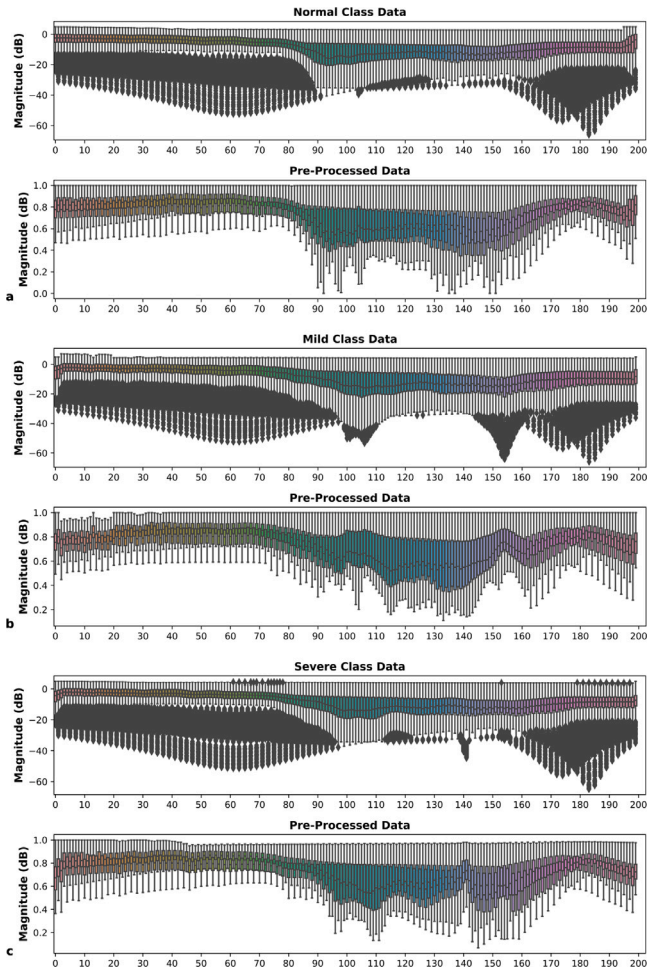

Fig. 4. Acquired original and pre-processed data after normalization and standardization where (a) show Normal class data (b) Mild class data (c) Severe class data.

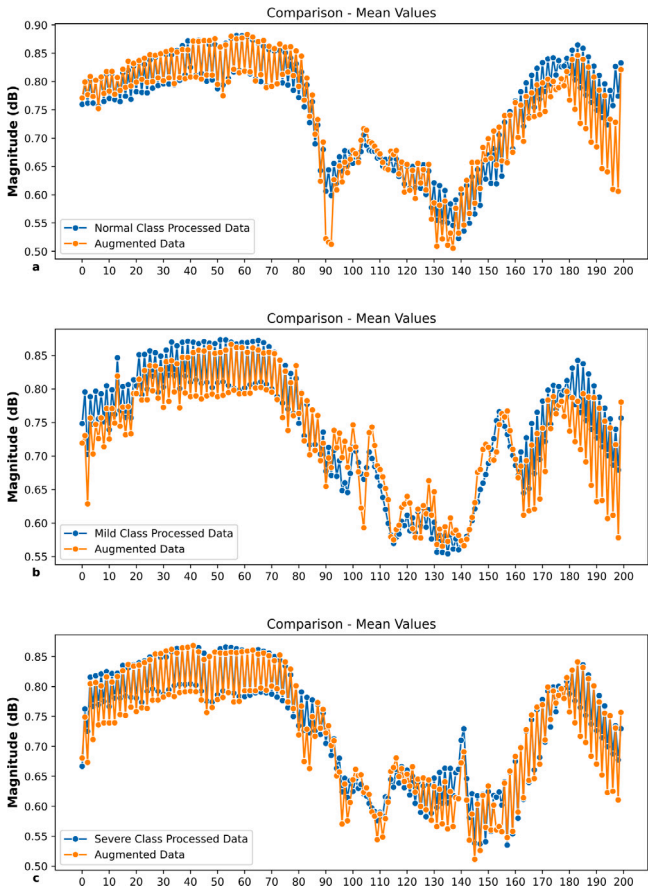

Fig. 5. Statistical augmentation process using Mean Value of preprocess and augmented data where (a) represents Normal class, (b) represents Mild class, (c) represents Severe class.

and model training. The graphical representations offered insights into data distribution and statistical features, highlighting the importance of each pre-processing step for rigorous scientific investigations.

The pre-processed data have fewer samples, which can be detrimental to the effectiveness of deep learning models that require a large sample size. To address this challenge, data augmentation is utilized to increase the amount of data available. This technique involves generating additional samples by introducing random variations to subsets of the original data, typically with a 1% difference. A comparison between the statistical properties of the pre-processed data and its augmented version is depicted in Fig. 5 represents the mean values at different intervals for various features, providing a clear visualization of the impact of data augmentation.

The outcomes underscore the efficacy of the data augmentation method in introducing variability into the dataset while maintaining the statistical integrity of the original data. By augmenting the dataset, this process expands its size and significantly improves its representativeness. This enhancement lays a robust foundation for the later stages of research, facilitating more comprehensive analyses and effective model training. The dataset becomes a more powerful tool for uncovering insights and achieving accurate classification results through this augmentation.

During the feature selection phase, the RFE Model was used in conjunction with Random Forest to pinpoint the most relevant features in the dataset. The main goal was to improve accuracy while keeping computational efficiency in check. After extensively testing different

Table 5
Different combinations of features using RFE model with random forest algorithm.

Feature selection	Algorithms	Number of features	Accuracy
RFE	RF	200	93%
		175	98%
		150	99%

numbers of features selected through the RFE model, it was decided to keep 150 features from the dataset, which produced the best outcomes as shown in Table 5.

Fig. 6 provides a visual representation of the original set of features against those selected through the RFE process, highlighting the effectiveness of the model in making accurate predictions. The strategic application of the RFE-Random Forest combination within this study presents an efficient and effective approach to improving the performance of the model. Notably, this methodology achieved an impressive accuracy rate of 99% during the feature selection phase, underscoring the method's efficacy in enhancing the predictive capabilities of the research model.

After employing the RFE model for feature selection, the PCA was used for feature extraction on the RFE-identified features. This step was aimed at addressing the high dimensionality of the dataset by efficiently condensing essential information, thereby maintaining significant patterns while minimizing complexity. Through PCA, a varying number of features were distilled, with the SelectKBest method subsequently applied to determine the most informative 125, 100, and 75 features.

The robustness and effectiveness of our approach were further validated by deploying a Random Forest Regression (RFR) model, which confirmed our methodology's precision in predicting the target variable

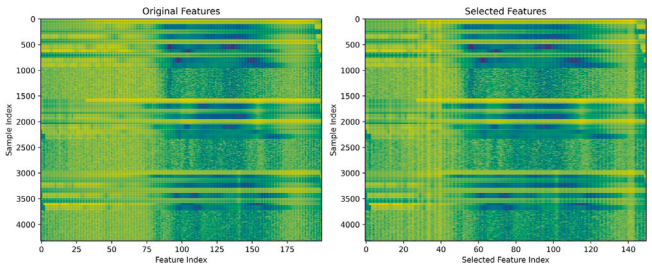

Fig. 6. RFE model to eliminate unwanted features where the first image presents dataset all features while the second image presents select features using RFE.

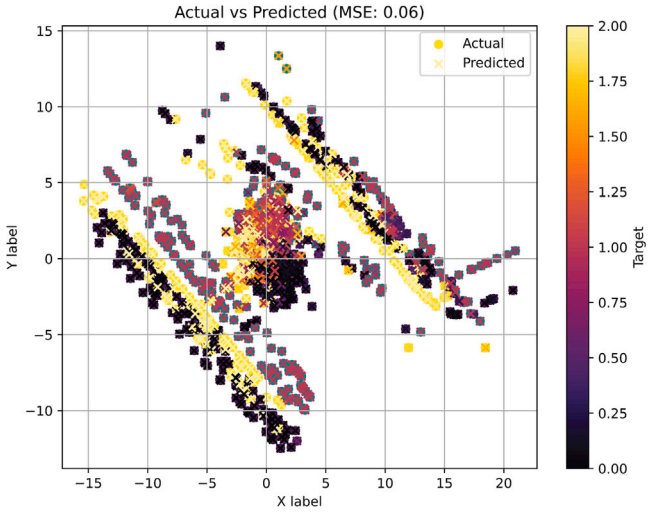

Fig. 7. Comparison of actual and predicted data using PCA with 100 features. The scatter plot illustrates the correlation between actual and predicted values, with color indicating feature intensity across 100 features. Mean squared error (MSE) is noted as 0.06.

Table 6
Different combinations of features using PCA model with random forest regressor algorithm.

	Algorithm	Best features	MSE	Accuracy
PCA	RFR	125	0.13	81.3%
		100	0.6	94.4%
		75	0.9	89.2%

with a minimal Mean Squared Error (MSE), as detailed in Table 6. Notably, the selection of the top 100 features yielded particularly compelling results, achieving an MSE of 0.6 and an accuracy rate of 94.4%, as illustrated in Fig. 7. These outcomes highlight the efficacy of our feature extraction process, offering significant contributions to the field by elucidating approaches to manage the challenges presented by high-dimensional datasets in regression analyses.

In this study, three distinct feature sets (100, 40, and 20 features) were utilized with two different feature extraction methods: RFE and PCA. The AE was then applied to refine the features, varying the AE features across 100, 40, and 20 dimensions. The AE architecture used was a 128-64-32-16-32-64-128 structure trained with Adam optimizers. The entire process involved 200 epochs and a batch size of 32. The results are summarized in Table 7 and Fig. 8.

For the RFE-AE method with 100 features, the Mean Squared Error (MSE) achieved was 7.05×10^{-3} for training and 7.98×10^{-3} for testing. Similarly, for the RFE-PCA-AE method with 40 features, the MSE values were 1.17×10^{-6} for training and 2.30×10^{-6} for testing. The findings indicate that RFE-PCA-AE outperforms RFE-AE, showcasing lower MSE values. Based on these results, we conclude that the PCA-AE method

Table 7
Results of different combinations of features using RFE-AE model and RFE-PCA-AE.

Train/Test	Epochs	Architecture	Error measures	
			RFE-AE	RFE-PCA-AE
Training	200	128-64-32-16-32-64-128	7.05×10^{-3}	1.85×10^{-6}
			7.98×10^{-3}	2.50×10^{-6}
Testing			1.02×10^{-2}	1.17×10^{-6}
			1.08×10^{-2}	2.30×10^{-6}
			1.11×10^{-2}	2.23×10^{-3}
			1.16×10^{-2}	2.55×10^{-3}

Table 8
Performance metrics of different classifier algorithms across multiple classes.

Algorithms	Class	Accuracy	Precision	Recall	F1-score
CNN-GRU	0	87%	87%	85%	86%
	1		85%	92%	89%
	2		88%	84%	86%
CNN-Bidirectional LSTM	0	83%	84%	82%	83%
	1		84%	87%	86%
	2		82%	82%	82%
CNN-LSTM	0	82%	84%	82%	83%
	1		81%	82%	82%
	2		81%	82%	81%

with 40 features exhibits the best performance, demonstrating minimal reconstruction error. Consequently, RFE-PCA-AE will be selected for further processing in subsequent classification tasks.

The classification results reveal significant variations in performance among different algorithmic combinations. CNN+GRU stands out as the top performer, with an impressive accuracy of 87%. Coming in second is the CNN+Bidirectional LSTM combination, which achieved a commendable accuracy of 83%. In contrast, the CNN+LSTM combination had a slightly lower accuracy score of 82%. In terms of precision, CNN+GRU again takes the lead with 87%, showing its ability to effectively classify instances while minimizing false positives. The CNN+Bidirectional LSTM combination follows suit with a precision score of 84%, indicating its reliability in correctly identifying positive instances.

Similarly, CNN+LSTM maintains competitive precision scores, albeit slightly lower at 82%. Regarding recall, CNN + GRU and CNN + bidirectional LSTM achieved recall scores of 87% and 83%, respectively. CNN+LSTM lags slightly behind in this aspect, with a recall score of 82%. When evaluating the F1 score, which balances precision and recall, CNN+GRU outperforms the other combinations with a score of 87%, highlighting its robustness in achieving a balance between accurate classification and minimizing false positives and negatives. CNN+Bidirectional LSTM and CNN+LSTM achieved F1-scores of 83% and 82%, respectively. Overall, CNN+GRU emerges as the most effective algorithmic combination in terms of accuracy and precision, closely followed by CNN+Bidirectional LSTM, while CNN+LSTM demonstrates respectable performance across all metrics, as shown in Fig. 9 and Table 8.

4.1. Discussion and comparative analysis

Neurodegenerative disorders such as AD pose a major global health challenge and are one of the leading causes of mortality. These conditions cause the brain's neuronal connections to break down and cause cognitive abilities to deteriorate gradually, affecting more than 50 million people worldwide. The prevalence of these diseases is expected to increase as the global population ages. AD, the most common form of dementia, is especially concerning, with affected individuals typically living for only three to nine years. Brain atrophy, characterized by a reduction in brain volume over time, is a notable physiological symptom of AD. The illness, which begins in a moderate preclinical stage and progresses to mild cognitive impairment, is characterized by

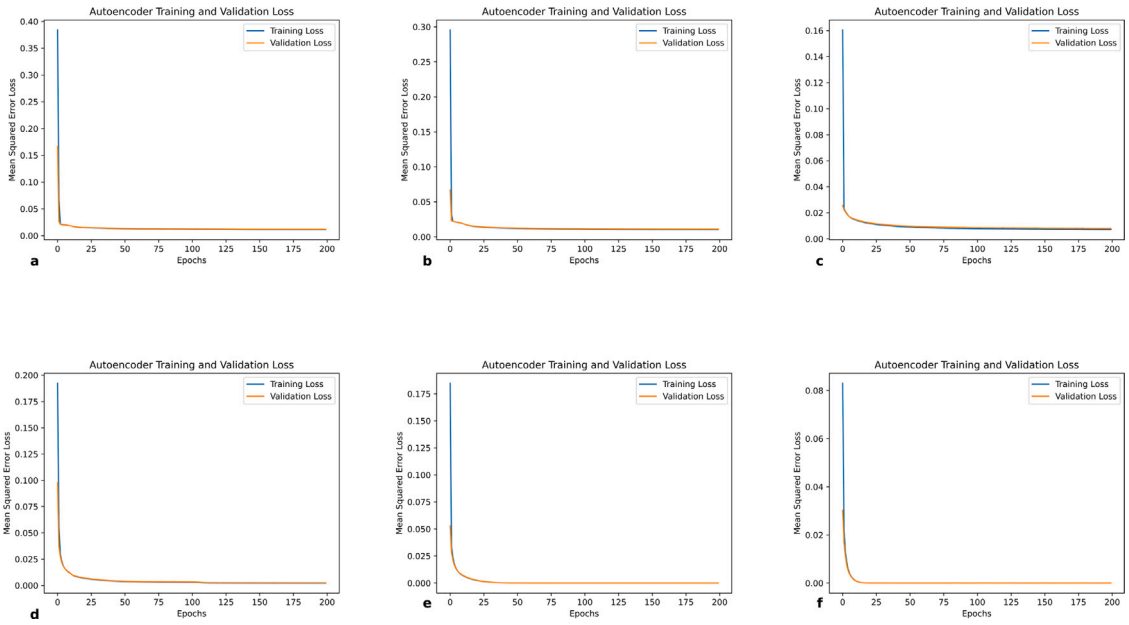

Fig. 8. Different combinations of AE, (a) shows RFE- AE with 20 (b) shows RFE- AE with 40 features (c) shows RFE- AE with 100 features (d) shows RFE- PCA-AE with 20 features (e) shows RFE- PCA-AE with 40 features (f) shows RFE- PCA-AE with 100 features.

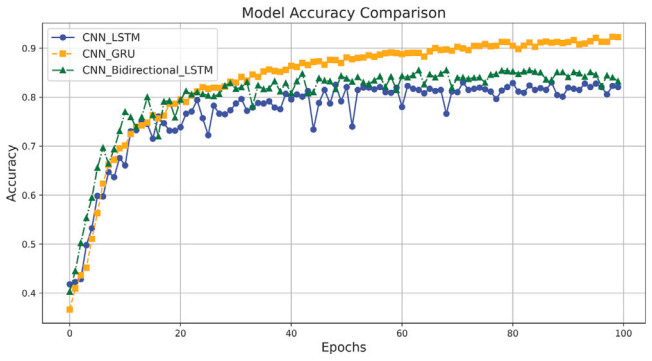

Fig. 9. Model accuracy comparison over 100 epochs using RFE-PCA-AE data. The graph displays the performance of three different neural network models—CNN-LSTM, CNN-GRU, and CNN-Bidirectional LSTM—highlighting their accuracy rates across training epochs.

the buildup of plaques and tangles in the brain, resulting in a decline in cognitive performance. In advanced stages, cognitive functions are severely affected, making independent living difficult and placing a significant burden on caregivers. As a result, AD is among the most economically burdensome diseases.

To improve treatment outcomes and reduce costs, early diagnosis, and effective monitoring are essential. Wearable and portable medical gadgets have attracted increasing attention in recent years, and they use microwave-based technology for various applications. While extensively studied for detecting conditions like breast cancer and stroke, recent research has shown that there are distinct differences in the dielectric properties of healthy brain tissues and those affected by AD. Microwave technology has been explored to monitor these changes in the brain, and promising results have been obtained. However, due to its low spatial resolution, there are various challenges to be solved before it can be used in real-world clinical settings.

First, the spatial resolution limits of microwave imaging can make it difficult to detect subtle changes in brain structure, especially in the early stages of AD. While microwave radar offers a non-invasive and potentially cost-effective means of continuous monitoring, the technology currently lacks the resolution achieved by more conventional imaging methods such as MRI and CT scans. This limitation can hinder the early detection of AD, where minute changes in brain tissue composition and structure are critical.

Furthermore, the integration of microwave radar technology into wearable or portable devices presents another set of challenges. Ensuring consistent and accurate data collection in dynamic, real-world environments where patient movement and external interference may affect readings is crucial. Additionally, the development of such devices must consider user comfort and compliance, as well as the variability in individual anatomical structures.

To address these challenges, ongoing research and development are focusing on enhancing the spatial resolution of microwave imaging through advanced signal processing algorithms and antenna design improvements (Hamza, Koziel, & Pietrenko-Dabrowska, 2024). Collaborative efforts with biomedical engineers and neurologists are also crucial to refine the technology's sensitivity to changes specific to AD pathology. Moreover, the use of ML and DL techniques to analyze the complex data collected from these devices could further enhance their diagnostic capabilities.

The use of ML and DL techniques in healthcare has become widespread. Researchers have been paying increasing attention to using ML and DL to classify MRI and CT scan images in recent years. However, this research identified a gap in existing studies, as most of them focus on processed data sets and use DL methodologies. On the contrary, a previous study, Ullah, Dong et al. (2023), achieved an impressive accuracy of 83% using the ML Random Forest algorithm. Our proposed DL method outperforms previous ML algorithms, achieving an accuracy of 87% as shown in Table 9. This comparative analysis highlights the superiority of our DL approach, which improves classification accuracy and improves data understanding through innovative methods.

Table 9
Comparative analysis with previous work.

Study	Accuracy	Precision	Recall	F1 Score
Ullah, Dong et al. (2023)	83%	83%	83%	83%
Proposed	87%	87%	87%	87%

5. Conclusion and future work

This study introduces a novel deep-learning classification method that uses data from numerical phantoms designed to replicate various stages of AD. Several phantoms with differing mesh cell compositions were used in the simulations to accommodate variations in head sizes. The obtained data was then preprocessed using a thorough preprocessing strategy to ensure data quality. This includes normalization and standardization with Min-Max and Standard Scalers to enhance robustness. In addition, outliers were removed using two techniques: the interquartile range and Tukey's fences. To expand the dataset, a new data augmentation method was developed, adding 500 synthetic cases for each stage of AD. Feature selection was carried out by recursive feature elimination, which retained 150 essential features while eliminating less relevant ones. The feature extraction process then involved the analysis of the main components and the autoencoders. Two approaches were tested: directly applying RFE-selected features to AE and channeling RFE-selected features through PCA before AE. The findings indicated that the RFE-PCA-AE approach was superior, leading to the selection of an optimal feature list (RFE 150, PCA 100, AE 40) for further analysis. Employing this refined feature set, various classifiers demonstrated notable accuracy. In particular, combining the convolutional neural network (CNN) and the gated recurrent unit (GRU), using the RFE + PCA + AE features, achieved the highest accuracy rate of 87%. This DL classification method, which leverages microwave data, shows significant potential for early-stage AD monitoring. Future research will extend the evaluation of this method to include its application on additional deep learning transformer algorithms, aiming to validate further and enhance its diagnostic capabilities.

CRediT authorship contribution statement

Farhatullah: Writing – original draft, Visualization, Software, Methodology, Formal analysis, Data curation, Conceptualization. **Xin Chen:** Validation, Supervision, Project administration, Investigation, Formal analysis. **Deze Zeng:** Validation, Supervision, Project administration, Methodology, Investigation. **Rahmat Ullah:** Writing – review & editing, Validation, Methodology, Data curation, Conceptualization. **Rab Nawaz:** Writing – review & editing, Visualization, Methodology, Formal analysis. **Jiafeng Xu:** Visualization, Software, Methodology. **Tughrul Arslan:** Validation, Project administration, Investigation, Data curation, Conceptualization.

Declaration of competing interest

The authors declare that they have no known competing financial interests or personal relationships that could have appeared to influence the work reported in this paper.

Data availability

Data will be made available on request.

References

Anwar, U., Khan, S., Arslan, T., Russ, T. C., & Lomax, P. (2024). Radio frequency-enabled cerebral blood flow monitoring and classification using data augmentation and machine learning techniques. *IEEE Sensors Journal*.

Bloom, G. S. (2014). Amyloid-β and tau: the trigger and bullet in Alzheimer disease pathogenesis. *JAMA Neurology*, *71*(4), 505–508.

Cardinali, L., Spano, M., Gugliermino, M., Rodriguez-Duarte, D. O., Ricci, M., Tobon-Vasquez, J. A., et al. (2023). A microwave sensing system enhanced by a machine learning algorithm for alzheimer's disease early detection. In *2023 IEEE conference on antenna measurements and applications* CAMA, (pp. 723–727). IEEE.

Chen, G., Shah, P., Stang, J., & Moghaddam, M. (2019). Learning-assisted multimodality dielectric imaging. *Institute of Electrical and Electronics Engineers. Transactions on Antennas and Propagation*, *68*(3), 2356–2369.

Chen, Y., Zhou, T., Chen, Y., Feng, L., Zheng, C., Liu, L., et al. (2022). HADCNet: Automatic segmentation of COVID-19 infection based on a hybrid attention dense connected network with dilated convolution. *Computers in Biology and Medicine*, *149*, Article 105981.

Chiao, J.-C., Li, C., Lin, J., Caverly, R. H., Hwang, J. C., Rosen, H., et al. (2022). Applications of microwaves in medicine. *IEEE Journal of Microwaves*, *3*(1), 134–169.

Fei, X., Wang, J., Ying, S., Hu, Z., & Shi, J. (2020). Projective parameter transfer based sparse multiple empirical kernel learning machine for diagnosis of brain disease. *Neurocomputing*, *413*, 271–283.

Fhager, A., Candefjord, S., Elam, M., & Persson, M. (2018). Microwave diagnostics ahead: Saving time and the lives of trauma and stroke patients. *IEEE Microwave Magazine*, *19*(3), 78–90.

Guo, R., Lin, Z., Shan, T., Song, X., Li, M., Yang, F., et al. (2021). Physics embedded deep neural network for solving full-wave inverse scattering problems. *IEEE Transactions on Antennas and Propagation*, *70*(8), 6148–6159.

Guo, R., Song, X., Li, M., Yang, F., Xu, S., & Abubakar, A. (2019). Supervised descent learning technique for 2-D microwave imaging. *Institute of Electrical and Electronics Engineers. Transactions on Antennas and Propagation*, *67*(5), 3550–3554.

Hamza, M. N., Koziel, S., & Pietrenko-Dabrowska, A. (2024). Design and experimental validation of a metamaterial-based sensor for microwave imaging in breast, lung, and brain cancer detection. *Scientific Reports*, *14*(1), 16177.

Hossain, A., Islam, M. T., & Almutairi, A. F. (2022). A deep learning model to classify and detect brain abnormalities in portable microwave based imaging system. *Scientific Reports*, *12*(1), 6319.

Jo, T., Nho, K., & Saykin, A. J. (2019). Deep learning in Alzheimer's disease: diagnostic classification and prognostic prediction using neuroimaging data. *Frontiers in Aging Neuroscience*, *11*, 220.

Kerhet, A., Raffetto, M., Boni, A., & Massa, A. (2006). A SVM-based approach to microwave breast cancer detection. *Engineering Applications of Artificial Intelligence*, *19*(7), 807–818.

Li, Y., Cui, W.-G., Huang, H., Guo, Y.-Z., Li, K., & Tan, T. (2019). Epileptic seizure detection in EEG signals using sparse multiscale radial basis function networks and the Fisher vector approach. *Knowledge-Based Systems*, *164*, 96–106.

Li, L., Wang, L. G., Teixeira, F. L., Liu, C., Nehorai, A., & Cui, T. J. (2018). DeepNIS: Deep neural network for nonlinear electromagnetic inverse scattering. *Institute of Electrical and Electronics Engineers. Transactions on Antennas and Propagation*, *67*(3), 1819–1825.

Nichols, E., Szoeke, C. E., Vollset, S. E., Abbasi, N., Abd-Allah, F., Abdela, J., et al. (2019). Global, regional, and national burden of Alzheimer's disease and other dementias, 1990–2016: a systematic analysis for the Global Burden of Disease Study 2016. *The Lancet Neurology*, *18*(1), 88–106.

O'Loughlin, D., O'Halloran, M., Moloney, B. M., Glavin, M., Jones, E., & Elahi, M. A. (2018). Microwave breast imaging: Clinical advances and remaining challenges. *IEEE Transactions on Biomedical Engineering*, *65*(11), 2580–2590.

Origlia, C., Rodriguez-Duarte, D. O., Tobon Vasquez, J. A., Bolomey, J.-C., & Vipiana, F. (2024). Review of microwave near-field sensing and imaging devices in medical applications. *Sensors*, *24*(14), 4515.

Persson, M., et al. (2014). Microwave-based stroke diagnosis making global prehospital thrombolytic treatment possible. *IEEE Transactions on Biomedical Engineering*, *61*(11), 2806–2817.

Pokorny, T., Vrba, J., Fiser, O., Vrba, D., Drizdal, T., Novak, M., et al. (2023). On the role of training data for SVM-based microwave brain stroke detection and classification. *Sensors*, *23*(4), 2031.

Polanco, J. C., Li, C., Bodea, L.-G., Martinez-Marmol, R., Meunier, F. A., & Götz, J. (2018). Amyloid-β and tau complexity—towards improved biomarkers and targeted therapies. *Nature Reviews Neurology*, *14*(1), 22–39.

Rana, S. P., Dey, M., Tiberi, G., Sani, L., Vispa, A., Raspa, G., et al. (2019). Machine learning approaches for automated lesion detection in microwave breast imaging clinical data. *Scientific Reports*, *9*(1), 10510.

Rekanos, I. T. (2002). Neural-network-based inverse-scattering technique for online microwave medical imaging. *IEEE Transactions on Magnetics*, *38*(2), 1061–1064.

Rodriguez-Duarte, D. O., Origlia, C., Vasquez, J. A. T., Scapaticci, R., Crocco, L., & Vipiana, F. (2022). Experimental assessment of real-time brain stroke monitoring via a microwave imaging scanner. *IEEE Open Journal of Antennas and Propagation*, *3*, 824–835.

Saied, I. M., & Arslan, T. (2020). Noninvasive wearable RF device toward monitoring brain atrophy and lateral ventricle enlargement. *IEEE Journal of Electromagnetics, RF and Microwaves in Medicine and Biology*, *4*(1), 61–68.

Saied, I. M., Arslan, T., & Chandran, S. (2022). Classification of Alzheimer's disease using RF signals and machine learning. *IEEE Journal of Electromagnetics, RF and Microwaves in Medicine and Biology*, *6*(1), 77–85.

Saied, I., Arslan, T., Chandran, S., Smith, C., Spires-Jones, T., & Pal, S. (2020). Non-invasive RF technique for detecting different stages of Alzheimer's disease and imaging beta-amyloid plaques and tau tangles in the brain. *IEEE Transactions on Medical Imaging*, *39*(12), 4060–4070.

Saied, I., Bashri, M., Arslan, T., Smith, C., & Chandran, S. (2019). Dielectric measurements of brain tissues with Alzheimer's disease pathology in the microwave region. In *2019 IEEE international symposium on medical measurements and applications (meMeA)* (pp. 1–6). IEEE.

Sanghvi, Y., Kalepu, Y., & Khankhoje, U. K. (2019). Embedding deep learning in inverse scattering problems. *IEEE Transactions on Computational Imaging*, *6*, 46–56.

Singh, A., Mandal, B., Biswas, B., Chatterjee, S., Banerjee, S., Mitra, D., et al. (2024). Microwave antenna-assisted machine learning: A paradigm shift in non-invasive brain hemorrhage detection. *IEEE Access*.

Tsang, G., Xie, X., & Zhou, S.-M. (2019). Harnessing the power of machine learning in dementia informatics research: Issues, opportunities, and challenges. *IEEE Reviews in Biomedical Engineering*, *13*, 113–129.

Ullah, R., & Arslan, T. (2020). PySpark-based optimization of microwave image reconstruction algorithm for head imaging big data on high-performance computing and Google cloud platform. *Applied Sciences*, *10*(10), 3382.

Ullah, R., & Arslan, T. (2021). Parallel delay multiply and sum algorithm for microwave medical imaging using spark big data framework. *Algorithms*, *14*(5), 157.

Ullah, R., Dong, Y., Arslan, T., & Chandran, S. (2023). A machine learning-based classification method for monitoring Alzheimer's Disease using electromagnetic radar data. *IEEE Transactions on Microwave Theory and Techniques*, *71*(9), 4012–4026.

Ullah, R., Saied, I., & Arslan, T. (2021). Big data-machine learning processing of recorded radiofrequency physiological and pathological measurements to predict the progression of Alzheimer's disease. In *Proceedings of the IEEE Asia-Pacific microwave conference* APMC, (pp. 223–225). IEEE.

Ullah, R., Saied, I., & Arslan, T. (2022). Measurement of whole-brain atrophy progression using microwave signal analysis. *Biomedical Signal Processing and Control*, *71*, Article 103083.

Ullah, R., Saied, I., & Arslan, T. (2023). Microwave sensing dataset for noninvasive monitoring of ventricle enlargement due to Alzheimer's disease. *Data in Brief*, *47*, Article 109006.

Vishal, S., Sourabh, A., & Harkirat, S. (2011). Alois Alzheimer (1864–1915) and the Alzheimer syndrome. *Journal of Medical Biography*, *19*(1), 32–33.

Wei, Z., & Chen, X. (2018). Deep-learning schemes for full-wave nonlinear inverse scattering problems. *IEEE Transactions on Geoscience and Remote Sensing*, *57*(4), 1849–1860.

Wei, Z., & Chen, X. (2019). Physics-inspired convolutional neural network for solving full-wave inverse scattering problems. *Institute of Electrical and Electronics Engineers. Transactions on Antennas and Propagation*, *67*(9), 6138–6148.

Yu, W., Lei, B., Wang, S., Liu, Y., Feng, Z., Hu, Y., et al. (2022). Morphological feature visualization of Alzheimer's disease via multidirectional perception GAN. *IEEE Transactions on Neural Networks and Learning Systems*, *34*(8), 4401–4415.

Zhang, L., Su, G., Yin, J., Li, Y., Lin, Q., Zhang, X., et al. (2021). Bioinspired scene classification by deep active learning with remote sensing applications. *IEEE Transactions on Cybernetics*, *52*(7), 5682–5694.

Zhang, X., Wang, T., Luo, W., & Huang, P. (2020). Multi-level fusion and attention-guided CNN for image dehazing. *IEEE Transactions on Circuits and Systems for Video Technology*, *31*(11), 4162–4173.

Zhu, G., Bialkowski, A., Guo, L., Mohammed, B., & Abbosh, A. (2021). Stroke classification in simulated electromagnetic imaging using graph approaches. *IEEE Journal of Electromagnetics, RF and Microwaves in Medicine and Biology*, *5*(1), 46–53.

Zuo, Q., Wu, H., Chen, C. P., Lei, B., & Wang, S. (2024). Prior-guided adversarial learning with hypergraph for predicting abnormal connections in Alzheimer's disease. *IEEE Transactions on Cybernetics*.

Zuo, Q., Zhong, N., Pan, Y., Wu, H., Lei, B., & Wang, S. (2023). Brain structure-function fusing representation learning using adversarial decomposed-VAE for analyzing MCI. *IEEE Transactions on Neural Systems and Rehabilitation Engineering*.